New Energy Power System Dynamic Security and Stability Region Calculation Based on AVURPSO-RLS Hybrid Algorithm

Saniye Maihemuti [1,*], Weiqing Wang [1,*], Jiahui Wu [1], Haiyun Wang [1], Muladi Muhedaner [2] and Qing Zhu [3]

[1]   College of Electrical Engineering, Xinjiang University, Urumqi 830047, China
[2]   Student Affairs Department, Changsha University of Technology, Changsha 410114, China
[3]   Nari Technology Co., Ltd., Nanjing 211106, China
*   Correspondence: saniye0622@stu.xju.edu.cn (S.M.); wwq59@sina.cn (W.W.)

Abstract: Using a high proportion of new energy is becoming the development trend of the modern power industry, with broad application prospects and potential threats to power system operation safety. This paper proposes a hybrid adaptive velocity update relaxation particle swarm optimization algorithm (AVURPSO) and recursive least square (RLS) method to quickly estimate the DSSR boundary using hyper-plane expression. Firstly, the operating point data in the high-dimension nodal injection space are analyzed using the AVURPSO algorithm to identify the key generators, equivalent search space, and critical points, which have relatively great effects on transient angle stability. The hyper-plane expression of the DSSR boundary, which matches the critical points best, is finally fitted by the RLS approach. Hence, the adopted algorithm is applied to rapidly approximate the DSSR boundary by hyper-plane expression in power injection spaces. Finally, the proposed algorithm is validated using a simulation case study on three wind farm regions of the actual Hami Power Grid of China using the DIgSILENT/Power Factory software. Consequently, the mentioned method effectively captures the security stability boundary of the new energy power system and realizes the three-dimensional visualization space of DSSR. By leveraging the DSSR, the state analysis can be conducted rapidly on several parameters, including security and stability assessments in relation to various energy supply capabilities. Meanwhile, these indices are calculated offline and applied online. The findings of this investigation confirm the efficacy and accuracy of the suggested modeling used in the analyzed system, offering technical assistance ensuring the stability of the new energy power system. The DSSR allows the rapid analysis of several parameters, including security and stability assessments with various energy supply capabilities.

Keywords: wind power; new energy power system; AVURPSO; RLS; DSSR

1. Introduction

China is seeking to improve the deteriorating natural environment, alleviate the shortage of energy and fuel, build a clean, low-carbon, safe and efficient energy system, implement new energy replacement actions, deepen the reform of the power system, and establish a new power system with new energy as the mainstay [1,2]. China has abundant new energy resources and large storage capacity for economic and environmentally friendly new energy, and can meet the load requirements for the construction and exploration of new energy, propelling it to the forefront [3]. As a clean and pollution-free system, wind energy stands out among clean energy sources [4]. With the increasing proportion of wind turbines being connected to the grid, their high randomness and volatility are also introduced into the grid, thus posing new challenges to the stability and security of the system [5]. To minimize the operation cost of the system and improve operation security, modern power systems use high-voltage transmission lines with large transmission capacities to interconnect regional power grids. These interconnection systems can enhance the transmission efficiency of the system, allowing the better centralization of frequency

modulations during fluctuations, and facilitating assistance between interconnected systems [6]. Since regional power grids rely more closely on each other, once a fault occurs in a specific region, its strong connection with other power grids can trigger large-scale cascading failures across interconnected power grids. Consequently, ensuring system security is becoming increasingly important [7]. In addition, the stable operation of the system also impacts the wind generator itself. Voltage that is too low will lead to the low voltage crossing of the wind turbine, while too-high voltage can cause wind turbine faults and even off-grid operation [8]. Thus, analyzing the stability of large-scale new energy power systems is of significant practical importance [9].

The strong uncertainty of wind turbines leads to greater complexity and changeable operation conditions in the power grid, making security analysis of the system more challenging [10]. Moreover, due to the limited scope for the calculation and analysis of the system's operation status after a large accident, the system cannot meet the requirements of real-time online analysis. Since traditional power system security analysis methods show great limitations and conservatism, it is urgent to develop a new analysis method that can adapt to the current complex power system. The "security domain" method is a novel approach that was developed based on the point-by-point method, which considers the problem from the perspective of the domain and describes the region wherein generally safe and stable operation is possible. The relative relationship between system operation points and the security stability region (SSR) boundary can provide safety margin and optimal control information, leading to the more scientific and effective online real-time safety monitoring, defense, and control of power systems. In 1975, E. Hnyilicza et al. proposed a power system security region analysis method [11,12]. In relation to the overall level of the region, the security domain encompasses the range of boundaries that ensure the overall safe operation of the entire system [13]. The SSR outlines the continuity domain wherein the system can operate safely, which has good adaptability when the system's operation mode is constantly changing. Moreover, the safety domain method can be used to judge the safety state of the system as a whole—not only can the safety of the operating point be judged according to whether it is in the safety domain or not, but the operator can also obtain the safety margin in each direction and the optimal control direction with reference to the distance of the operating point in high-dimensional space to the boundary of the safety domain, which is important information to decision-making [14].

Therefore, the concept of the security stability region (SSR) is proposed to help develop a new method of power system stability analysis. The primary problem facing the construction of the SSR is the fast identification of the critical point of stable operation, and the forming of the boundary of the SSR [15]. Given the grid structure (topology and component parameters) and the expected fault conditions, the safety domain is uniquely determined in the node injection space, and thus can be calculated offline and applied online. Compared with the traditional "point-by-point" method, the safety domain approach is less computationally intensive and is faster, thus saving time for real-time decision analysis when applied in online safety assessment. Moreover, specific security and stability issues have led to the development of the static security stability region (SSSR), small disturbance security stability region (SD-SSR), and dynamic security stability region (DSSR) concepts. Among these, research on the SSSR in modern power systems has become relatively more mature than that on the latter two. On the contrary, after a given fault, the system remains safe and stable up to a certain power injection point on the injection space, and this operating point is called the stable operating point. The DSSR is the set of all stable operating points [16]. For a given fault, it is only necessary to determine whether its injected power point lies within the DSSR, and the safety margin of the system can be derived according to the relative position of this power point, which is convenient and can be applied online. At the same time, the operators can also develop corresponding control strategies and scheduling plans based on the relative positions of the power injection points, in order to achieve effective online safety evaluations and optimization. Currently, the more mature method for calculating DSR is the fitting method [17]. The fitting method is the most widely

used and mature method. The key to this proposed method is to obtain sufficient critical injection points via numerical simulation. Then, the bounding hyperplane is obtained by fitting it with the mathematical analysis method, the least squares method. Although this method has high computational accuracy, the time required to search for critical points is long, especially in relation to the increasingly complex and large-scale interconnected power grids, and the utility of the fitting method is greatly reduced here. On this basis, F. F. Wu proposed the concept of the inscribed hyperplane. The inscribed hyperplane is a subdomain of the DSSR, and the upper and lower constraints of node injection quantity describe its mapping relationship. Reference [18] proved that the boundary of the security region can be represented by a set of one or more hyperplanes in the field of engineering. Ref. [19] carried out a piecewise approximation of the boundary of the SSSR based on the relationship between the space angle of the space tangent vector at the critical point and the maximum space angle threshold. Reference [20] used the Taylor series trajectory sensitivity method to identify the security region. The above study aimed to improve the efficiency and accuracy of security domain construction. However, in the calculation of the DSSR, since the SSR boundary as a hyperplane and the injected power vector as spatial points can be formed, the following obviously holds. (1) When the power operating point is inside the SSR, if the point is further away from the SSR boundary, the system is safer; when the point is closer to the system boundary, it means that the system is closer to the critical state. (2) When the power operation point is outside the SSR, if the point is farther away from the SSR boundary, the system deviates from the steady state; when the point is closer to the system boundary, it means the system is closer to the critical state.

At present, China's power system is developing rapidly, and the conditions of regional interconnection, HVDC transmission, and north–south mutual supply have led to a more complex structure and increases in the scale of the power grid. In order to evaluate the safety and stability of the system after a fault, and to ensure the economy and safety of transmission and distribution, a transient stability simulation of the system is required. When DSSR is used to analyze the safety of large interconnected grids, a large number of numerical simulations are required. Due to the limitations of simulation conditions and practicality requirements, effective and appropriate DSSR simulations must be performed for large-scale power systems in order to reduce the computational effort and improve the practicality of the algorithm [21,22]. Refs. [23,24] provide a detailed analysis of the DSSR, and propose the following topological properties: (1) there is no "hole" inside the DSSR—as long as the injected power vector is inside the SSR, the system can remain transient and stable under perturbations; (2) there is no "island" outside the DSSR, and no "knot"—if the injected power vector is outside the SSR, it means that the injection will cause transient instability; (3) the boundary of the DSSR can be expressed as a concatenation of multiple directional surfaces, or as a common fit. The above properties provide an important reference for the dynamic full domain to be practically applied, such that in practical applications, as long as the SSR boundary is calculated, the system's state of stability can be judged by analyzing the relationship between the realistic power injection and the SSR boundary. On this basis, further quantitative analyses can be performed [25–28].

The fitting method calculates the dynamic safety domain by locating the critical operating points of the system through a large number of simulations of the system notation, and after obtaining a set of critical operating points, this point group is fitted to obtain the dynamic safety domain hyperplane boundary; the fitting method is generally least squares. The fitting method makes full use of the dynamic safety domain properties, is conceptually simple and intuitive, and is robust and easy to apply, while being computationally intensive [29,30]. The specific methods are as follows:

I.   Search for critical points—(1) Given the system topology, we seek the fault occurrence point, fault type, fault clearance time, and other basic parameters. (2) Given the injection vector y with calculated power initial value, the injection point is assessed in terms of whether it belongs to the critical injection point via the numerical simulation method or the direct method;

II.   The judgment of the critical point. When judging the critical injection power point, the critical point can be expressed as the point between the stable region and the unstable region, which is a kind of transition point;

III.   Fitting of critical surfaces. After selecting the critical point group for a particular case, the above approach requires screening. There are also studies that use some fast search hyperplane methods that can shorten the computation time while maintaining accuracy. In summary, the key to obtaining a DSSR boundary is to locate sufficient critical points as quickly as possible, and then fit them effectively. In particular, one must quickly locate critical points from a large number of operating points in the high-dimension nodal injection space.

Therefore, owing to the rapid development of artificial intelligence (AI) techniques [31,32] and the widespread deployment of new energy power systems, some intelligent optimization algorithms are also being used in power system analysis. However, this approach cannot guarantee accuracy in the global tracking of SSR critical points. Therefore, we have developed a general meta-heuristic algorithm to form the DSSR in a new energy power system. In recent years, the adaptive velocity update relaxation particle swarm optimization (AVURPSO) algorithm [33] and recursive least square (RLS) method [14] have shown significantly faster speed, higher accuracy, and widespread applicability, and can thus be complimentary to the model-based method. This study introduces an AVURPSO-RLS algorithm for identifying the critical security stability operation region of the new energy power system more quickly and accurately. A novel hybrid AVURPSO-RLS algorithm is proposed to search for the maximum dynamic security and stability operation region under the fault of N-1. Three cases of a Hami power grid (new energy power system) with different power outputs have been simulated in the DIgSILENT/Power Factory 15.1 software, and the DSSR of the system has been fitted and analyzed.

2. Mathematical Model of New Energy Power System

Figure 1 provides a high-level overview of the new energy power system architecture that has formed the basis of this investigation. The synchronous generator (SG) is the traditional power system. The doubly fed induction generator (DFIG) is connected to the large power grid through the point of common coupling (PCC) bus. The wind turbine (WT) and photovoltaic power (PV) make up the new energy power generation system. V_s is the balancing point of the system's voltage, and $\dot{V}_{pcc}$ represents the voltage of new energy farms at the PCC. The PCC is supplied with the following types of energy by the new energy farms (for example, $\dot{V} = V\angle 0°$, $\dot{V}_{pcc} = V_{pcc}\angle\theta$). Additionally, electrical supply systems are embedded with high penetration of new energy to provide the electricity load, and these are linked to the electricity network. As a result of the new energy power system, the stability and dependability of energy consumption are enhanced by switching between different sources of energy and utilizing their unique benefits.
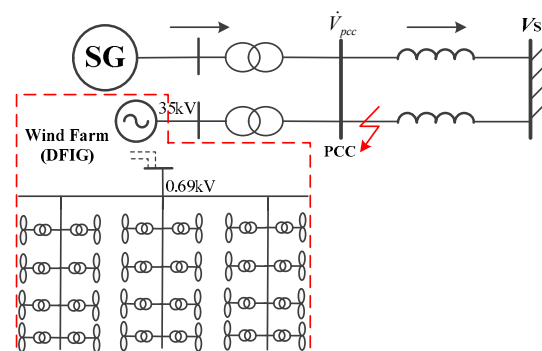

Figure 1. Grid connection system.

2.1. Power System Model

The paper considers a power network that includes both new energy power generation systems and traditional power generation systems. The PFC for this power system is consistent with the AC power flow of the traditional system. The nodal power deviation equation can be written as follows:

$$\Delta P_i = P_i^{\text{EG}} - P_i^{\text{ED}} - V_i \sum_{j \in i} V_j \left(G_{ij} \cos \theta_{ij} + B_{ij} \sin \theta_{ij} \right) \tag{1}$$

$$\Delta Q_i = Q_i^{\text{EG}} - Q_i^{\text{ED}} - V_i \sum_{j \in i} V_j \left(G_{ij} \cos \theta_{ij} - B_{ij} \sin \theta_{ij} \right) \tag{2}$$

where P_i and Q_i are injected active power and reactive power, respectively. Moreover, θ_{ij} indicates the corresponding voltage phase angle difference between i and j. P_i^{EG} and Q_i^{EG} represent the injection powers; P_i^{ED} and Q_i^{ED} are the energy consumed by the bus i electrical load. V_i and V_j denote the voltage of bus i and j. Finally, G_{ij} and B_{ij} are the conductance and admittance, respectively.

Voltage fluctuations occur due to system disturbances or when the voltage command is altered by dispatching at a higher level. In this case, power systems must adhere to the following voltage deviation limits from the grid point:

$$V_{\text{pcc}}^{\text{ref}} - V_{\text{pcc}}^{\text{err}} \leq V_{\text{pcc}} \leq V_{\text{pcc}}^{\text{ref}} + V_{\text{pcc}}^{\text{err}} \tag{3}$$

$$[Q_{g_{i\min}}, Q_{g_{i\max}}] = \begin{cases} [0, Q_{g_{i\max}}], V_{\text{pcc}}^{\text{ref}} > V_{\text{pcc}} + V_{\text{pcc}}^{\text{band}} \\ [Q_{g_{i\min}}, 0], V_{\text{pcc}}^{\text{ref}} < V_{\text{pcc}} - V_{\text{pcc}}^{\text{band}} \end{cases} \tag{4}$$

where V_{pcc} is the current voltage, $V_{\text{pcc}}^{\text{ref}}$ indicates the voltage control instruction, $V_{\text{pcc}}^{\text{err}}$ represents the voltage error, and $V_{\text{pcc}}^{\text{band}}$ represents the voltage control dead zone.

$$U_{i\min} \leq U_i \leq U_{i\max} \qquad i \in N_{\text{S}} \tag{5}$$

$$Q_{\text{sc}_{i\min}} \leq Q_{\text{sc}_i} \leq Q_{\text{sc}_{i\max}} \qquad i \in N_{\text{Q}} \tag{6}$$

where $V_{i\max}$ and $V_{i\min}$ are the upper and lower limits of the voltage, respectively.

2.2. Uncertainty Model of Wind Power Output

The probability model of the wind turbine comprises two components: the wind speed model and the wind turbine model. Wind speed is affected by different factors, such as region, season, climate temperature, and geographical location, and has strong random volatility. When analyzing the PFC of the power system with new energy, the active output of the wind farm is calculated using the fan output characteristic curve. Wind speed is described by the high-precision fitting of the Weibull Distribution of wind speed change. Its PDF is shown in Figure 2.

During operation, an asynchronous generator is typically used with an inverter to generate an excitation magnetic field, which enables it to realize reactive power absorption and maintains the stable operation of the power grid. The probability model of wind turbine output power can be expressed as follows:

$$f_{P_{\text{W},t}}(P_{\text{W},t}) = \begin{cases} \Pr(P_{\text{W}_t} = 0) = 1 - \exp(-(\frac{WS_{\text{in}}}{c_t})^{k_t}) + \exp(-(\frac{WS_{\text{off}}}{c_t})^{k_t}) \\ \Pr(P_{\text{W}_t} = P_{\text{WR}} = \exp(-(\frac{WS_{\text{R}}}{c_t})^{k_t}) - \exp(-(\frac{WS_{\text{off}}}{c_t})^{k_t}) \\ \frac{k_t(WS_{\text{R}} - WS_{\text{in}})}{c_t^{k_t} * P_{\text{WR}}} \left[WS_{\text{in}} + \frac{P_{\text{W}_t}}{P_{\text{WR}}} (WS_{\text{R}} - WS_{\text{in}}) \right]^{k_t - 1} * \exp\left[-(\frac{WS_{\text{in}} + (P_{\text{W}_t}/P_{\text{WR}}) * (WS_{\text{R}} - WS_{\text{in}})}{c_t})^{k_t - 1} \right], \text{else} \end{cases} \tag{7}$$

$$(P_{W_{i,\text{tur},t}} - P_{W_{i,t}}) = \int_{P_{W_{i,t}}}^{P_{WR_i}} (P_{W_t} - P_{W_{i,t}}) f_{P_{W_t}}(P_{W_t}) d(P_{W_t}) + \Pr(P_{W_t} = P_{WR}) * (P_{WR} - P_{W_{i,t}})$$
$$(P_{W_{i,t}} - P_{W_{i,\text{tur},t}}) = \int_{0}^{P_{W_{i,t}}} (P_{W_{i,t}} - P_{W_t}) f_{P_{W_t}}(P_{W_t}) d(P_{W_t}) + \Pr(P_{W_t} = 0) * P_{W_{i,t}} \tag{8}$$

where WS_{in} is the cut in wind speed, WS_{off} symbolizes cut out wind speed, WS_R denotes rated wind speed, and P_{WR} represents rated output power. In addition, k_t is the shape parameter at time t, and c_t is the scale parameter reflecting the average wind speed of the wind field, m/s. $P_{Wi,t}$ is the actual output of ith wind farm at t time.
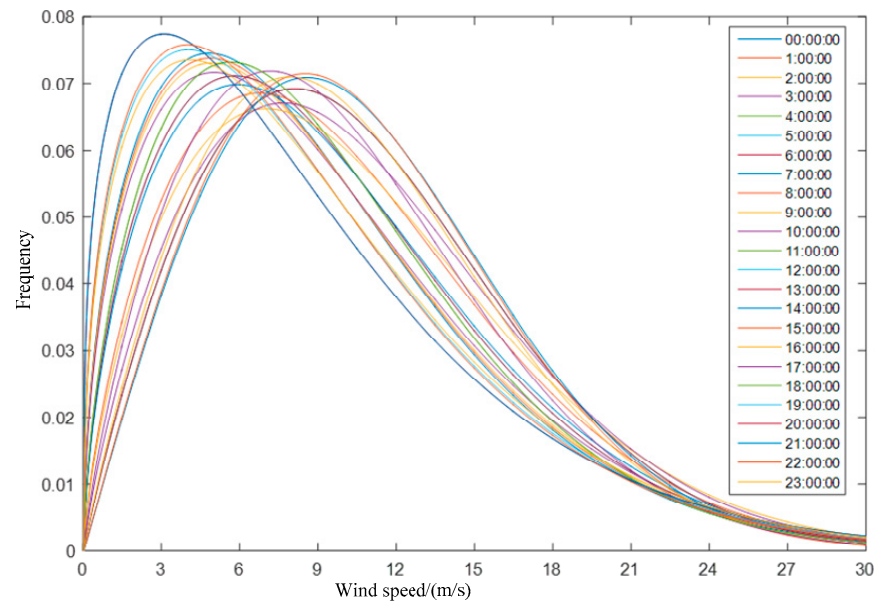

Figure 2. The PDF of wind speed in 24 h.

3. Mathematical Model of DSSR

A power system's DSSR is a node injection power space comprising the active and reactive power injected by all power system nodes. The boundary of a dynamic security and stability margin is uniquely determined by the network topology of the system, and remains constant regardless of the operating state, such as node injection. The DSSR boundary only needs to be calculated once for the given network topology and a predetermined contingency value. Then, its hyperplane coefficient is stored in the database for online use in the future, without increasing the computational burden of online use.

3.1. Security Constraints and SSR of the Grid

The grid nodes are divided into generator G and load L. The voltage limitation set is specified as follows:

$$\mathfrak{M}_{Vr} := \mathfrak{M}_{V(L)r} \times \mathfrak{M}_{V(G)r} \tag{9}$$

Among these,

$$\mathfrak{M}_{V(L)} := \left\{ V_L \,\middle|\, V_L^{\min} \leq V_L \leq V_L^{\max} \,\middle|\, V_L \in R^{(n-n_0)} \right\} \tag{10}$$

$$\mathfrak{M}_{V(G)} := \left\{ V_G \,\middle|\, V_G^{\min} \leq V_G \leq V_G^{\max} \,\middle|\, V_G \in R^{n_0} \right\} \tag{11}$$

Letting $\Theta_k^M = \alpha_i - \alpha_j$ be the voltage phase angle variation between nodes i and j at both ends of the branch, the power system's line current limitation can be presented as follows:

$$\mathfrak{M}_{\Theta r} := \mathfrak{M}_{\Theta(TB)} \times \mathfrak{M}_{\Theta(LB)} \tag{12}$$

Among these,

$$\mathfrak{M}_{\Theta(TB)} := \left\{ \Theta_{TB} \middle| -\Theta_{TB}^M \le \Theta_{TB} \le \Theta_{TB}^M \right\} \tag{13}$$

$$\mathfrak{M}_{\theta(LB)} := \left\{ \Theta_{LB} \middle| -\Theta_{LB}^M \le \Theta_{LB} \le \Theta_{LB}^M \right\} \tag{14}$$

$$\Theta_{TB} \in R^n, \Theta_{LB} \in R^{n_b - n} \tag{15}$$

Suppose P_i^M and P_i^m represent the maximum and the minimum permissible limits of P_i. In this case, the constraint set satisfying (V, Θ) is as follows:

$$\mathfrak{M}_P := \left\{ (V, \Theta) \middle| P_i^m \le P_i(V, \Theta) \le P_i^M, i \in G \right\} \tag{16}$$

Among these,

$$V = \begin{pmatrix} V_G \\ V_L \end{pmatrix}, \ \Theta = \begin{pmatrix} \Theta_{TB} \\ \Theta_{LB} \end{pmatrix} \tag{17}$$

The set $\mathfrak{M}$ described by the coordinates (V, Θ) can be represented as follows:

$$\mathfrak{M}_{V(L)r} := \begin{cases} \Delta V_L \in R^{n-n_0} \\ V_L^m - V_L^0 \le \Delta V_L \le V_L^M - V_L^0 \end{cases} \tag{18}$$

$$\mathfrak{M}_{V(G)r} := \begin{cases} \Delta V_G \in R^{n_0} \\ V_G^m - V_G^0 \le \Delta V_G \le V_G^M - V_G^0 \end{cases} \tag{19}$$

3.2. DSSR Boundary of Power System

There are two hypotheses regarding the SSR of the power grid [18], as follows:

Hypothesis 1. *Only the DSSR of active power needs to be studied.*

Hypothesis 2. *In the injected power space, the DSSR must satisfy the following inequality because the active power injection of the generator P_u is always positive, and the active power injection of the load P_v is always negative:*

$$P_u \ge 0, \ P_v \le 0 \tag{20}$$

The structure of a power system with short-circuit fault can be divided into three stages: Before, during, and after the accident.

$$\begin{cases} \frac{dx}{dt} = f_a(x), \ -\infty < t < 0 \\ \frac{dx}{dt} = f_b(x), \ 0 < t < \tau \\ \frac{dx}{dt} = f_c(x), \ \tau < t < +\infty \end{cases} \tag{21}$$

where a, b, and c represent the pre-fault, fault-time, and post-fault network topologies, respectively, and τ is the time constant for the short circuit fault.

After a specific type of short-circuit defect, the given power system's architecture is transiently stable if the injected power vector y (including the active power injection P_i of three units) is stable. Dynamic security stability describes this condition, and the injected power y is safe. In the realm of injected power, the DSSR looks like this:

$$\Omega_d(a, b, c) := \{ \boldsymbol{y} \middle| \boldsymbol{x}_d(\boldsymbol{y}) \in A(\boldsymbol{y}) \} \cap Y_l \tag{22}$$

where $x_d(y)$ is the fault-clearing state, A(y) indicates the SSR around the equilibrium point given by injection y in the state space after the fault, and Y_l is the constraint set of the maximum and minimum limits of the injection power space of each node.

3.3. Hyperplane Equation Construction

The DSSR is composed of critical hyperplanes, and the hyperplane equation can be expressed as follows:

$$\sum_{s=1}^{n} \alpha_s P_s = 1 \tag{23}$$

where P_s is the system's sth active power injection, and α_s indicates the hyperplane coefficient that corresponds to P_s.

According to hyperplane approximation, the DSSR can be expressed as follows:

$$\Omega_d := \left\{ P \in R^n \left| \begin{array}{c} \sum\limits_{s=1}^{n} \alpha_s P_s \leq 1 \\ P_s^m \leq P_s \leq P_s^M \end{array} \right. \quad s = 1, 2, \cdots, n \right\} \tag{24}$$

The following equation is the DSSR boundary fitting error:

$$Err_{DSR} = \frac{\left| \sum\limits_{i=1}^{n} \alpha_i P_i - 1 \right|}{\sqrt{\sum\limits_{i=1}^{n} \alpha_i^2} \cdot \sqrt{\sum\limits_{i=1}^{n} P_i^2}} \tag{25}$$

4. Study of the AVURPSO-RLS Approach for Hyperplane Fitting

This paper combines the intercept and AVURPSO-RLS methods to calculate the hyperplane coefficient of the security domain and then obtain the DSSR of the new energy power system.

4.1. AVURPSO Algorithm

The novelty of the present study lies in finding the global optimum of the injection power value at the best level using an adaptive velocity update relaxation particle swarm optimization, namely, AVURPSO, with a higher convergence speed and more accurate response than the basic particle swarm optimization (PSO) algorithm seen in Figure 3. The individuals of the PSO algorithm are referred to as particles, and the positions of particles within the search space are changed based on each of the individuals' social–psychological tendencies to delete others. Specifically, the velocity (v) and position (x) of each particle will be changed by the particle's best value (P_{best}) and the global best value (G_{best}), as follows:

$$v_i(j+1) = \omega \cdot v_i(j) + c_1 \cdot r_1 \cdot (P_{best}(j) - x(j)) + c_2 \cdot r_2 \cdot (G_{best}(j) - x(j)) \tag{26}$$

$$x_i(j+1) = x_i(j) + v_i(j+1) \tag{27}$$

$$\omega = \omega_{max} - \left(\frac{\omega_{max} - \omega_{min}}{i_{ter,max}} \right) \tag{28}$$

where $v_i(j+1)$ represents particle i's velocities at iteration j, and $x_i(j+1)$ indicates particle i's locations at that iteration. Moreover, ω is the inertia weight used to regulate the effect of past velocity history. In this equation, t represents the number of iterations, c_1 represents the learning factor for cognitive abilities, c_2 is the learning factor for social abilities, and r_1 and r_2 are random values with uniform distribution across [0, 1]. Particles' uncontrolled excursions beyond the search space may often be quelled by limiting the value of each component in v to fall inside the interval [v_{min}, v_{max}]. Typically, particles' velocities in classic PSO are capped at a value between [v_{min}, v_{max}]. The default values for v_{min} and v_{max} are x_{min} and x_{max}, respectively. The particle locations are listed inside the interval [x_{min}, x_{max}].
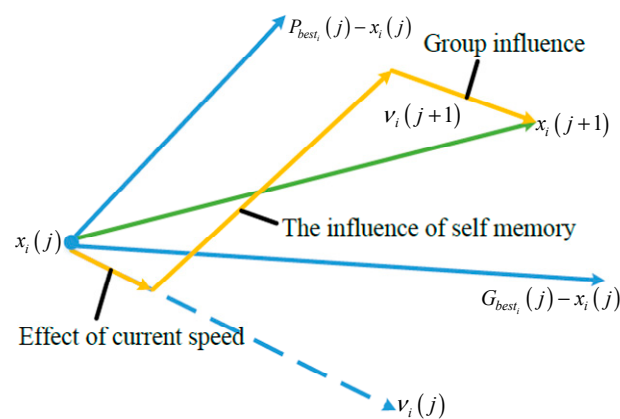
Figure 3. Search criteria in standard PSO algorithm.

In AVURPSO, the velocity of each particle remains unchanged if its fitness at the current iteration is superior to that at the preceding iteration. Otherwise, the particles' velocities are updated as stated by [28], thereby improving computational efficiency. The new position of the particle is then calculated by [33]:

$$x_i(j+1) = (1 - mf)x_i(j) + (mf)v_i(j+1) \tag{29}$$

If c_1 and c_2 are kept modest, the particle may travel a greater distance before being dragged back. In contrast, using high values accelerates progress, but may compromise the ability to reach the designated areas. Therefore, c_1 and c_2 are presented as:

$$c_1 = \frac{(iter_{\max} - iter) \times (c_{1b} - c_{1a})}{iter_{\max}} + c_{1a} \tag{30}$$

$$c_2 = \frac{(iter_{\max} - iter) \times (c_{2b} - c_{2a})}{iter_{\max}} + c_{2a} \tag{31}$$

where c_{1b} and c_{2b} are the beginning and ending values of constants c_1 and c_2, and c_{1a} and c_{2a} are the constants' intermediate values. In reality, the optimal solutions are usually identified throughout the search interval, including values for c_1 from 2.5 to 0.5 and c_2 from 0.5 to 2.5. When c_1 is set to a high value and c_2 is set to a small value, particles are free to roam the search space rather than converging on the $(P_{best})_i$. Late in the optimization, when c_1 is small and c_2 is big, the particles converge to $(G_{best})_i$. The convergence speeds of PSO and AVURPSO algorithms are shown in Figure 4.
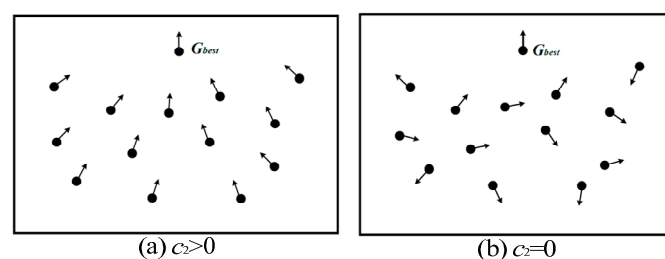

Figure 4. Convergence speeds of PSO and AVURPSO algorithms.

The momentum factor, *mf*, has a value between 0 and 1. Take the following equation as an example of an adaptive modification made to the momentum factor:

$$mf = \frac{(iter_{\max} - iter) \times (mf_2 - mf_1)}{iter_{\max}} + mf_1 \tag{32}$$

where *mf* is decreased from the maximum value mf_1 to the minimum value mf_2.

As shown in Figure 5, the objective function for G_{best} converges in the PSO, IPSO, VURPSO and AVURPSO algorithms. This figure shows that using the PSO as an objective function leads to convergence values of 0.00334, 0.00335, 0.00325, and 0.00323 for G_{best} in the PSO, IPSO, VURPSO and AVURPSO algorithms, respectively. Therefore, AVURPSO is a superior algorithm to the other three. The following shows summaries of the case studies presented in this paper.
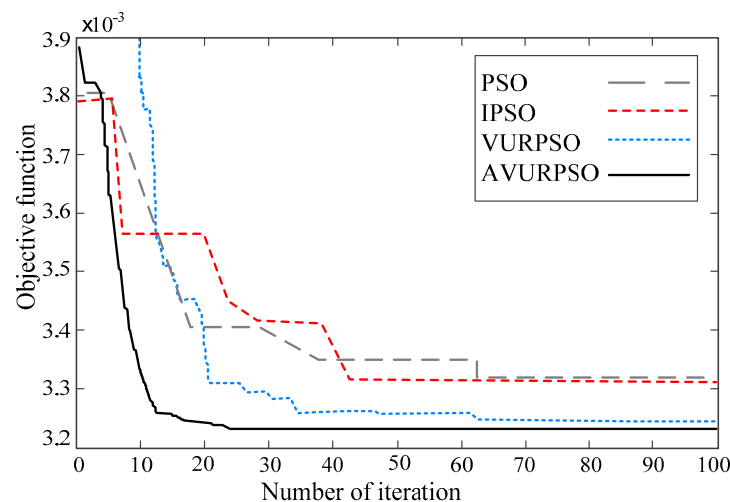
Figure 5. Convergences of the objective function for G_{best}.

4.2. Recursive Least Square (RLS) Method

The least square (LS) method is the most basic and widely used method, and was first proposed by Gauss (k. f. Gauss) in his research on orbital motion orbit prediction. The RLS is a newly developed method based on the LS method [14]. The RLS can be obtained as follows:

To represent the L-group observations of an observable system, the symbol $\{y_i \in R, y_i \in R^n, i = 1, 2, \ldots, L\}$ is used to satisfy $y_i = x_i \theta$ as below:

$$\begin{bmatrix} y_1 \\ y_2 \\ \vdots \\ y_k \end{bmatrix} = \begin{bmatrix} \phi_1^T \\ \phi_2^T \\ \vdots \\ \phi_k^T \end{bmatrix} \Theta \tag{33}$$

where *k* represents *k* groups of observed data; y_i represents the output observation of the *i*th group of data. $\phi_i^T = \begin{bmatrix} x_1^i, x_2^i, \cdots, x_n^i \end{bmatrix} \in R^{1 \times n}$; $\Theta = \begin{bmatrix} \theta_1 \\ \theta_2 \\ \vdots \\ \theta_n \end{bmatrix} \in R^{n \times 1}$ indicates the input observation value of the *i*th group of data.

where $\Phi_k = \begin{bmatrix} \phi_1^T \\ \phi_1^T \\ \vdots \\ \phi_1^T \end{bmatrix} \in R^{k \times n}$, $Y_k = \begin{bmatrix} y_1 \\ y_2 \\ \vdots \\ y_n \end{bmatrix} \in R^{k \times 1}$

Φ is the data vector matrix and Y is the system output matrix.

From this, at time *k*, the least squares estimate can be obtained.

$$\hat{\Theta} = \left(\Phi_k^T \Phi_k \right)^{-1} \Phi_k^T Y_k \tag{34}$$

where

$$P_k^{-1} = \Phi_k^T \Phi_k \tag{35}$$

because

$$P_k^{-1} = \Phi_k^T \Phi_k = [\phi_1, \phi_2, \cdots, \phi_k] \begin{bmatrix} \phi_1^T \\ \phi_2^T \\ \vdots \\ \phi_k^T \end{bmatrix} = \sum_{i=1}^n \phi_i \phi_i^T = \sum_{i=1}^{n-1} \phi_i \phi_i^T + \phi_k \phi_k^T = P_{k-1}^{-1} + \phi_k \phi_k^T \tag{36}$$

Therefore,

$$P_k^{-1} = P_{k-1}^{-1} + \phi_k \phi_k^T \tag{37}$$

$$\Phi_k^T y_k = \Phi_{k-1}^T y_{k-1} + \phi_k y_k \tag{38}$$

$$\hat{\Theta}_k = \left(\Phi_k^T \Phi_k \right)^{-1} \Phi_k^T y_k = P_k \Phi_k^T y_k = P_k \left(\Phi_{k-1}^T y_{k-1} + \phi_k y_k \right) \tag{39}$$

because

$$\hat{\Theta}_{k-1} = P_{k-1} \Phi_{k-1}^T y_{k-1} \tag{40}$$

Therefore,

$$P_k^{-1} \hat{\Theta}_k = \phi_k \phi_k^T \tag{41}$$

At time *k*, this can be expressed as

$$\begin{aligned} \hat{\Theta}_k &= P_k \left(\Phi_{k-1}^T y_{k-1} + \phi_k y_k \right) = P_k \left(P_k^{-1} \hat{\Theta}_{k-1} + \phi_k y_k \right) = P_k \left(P_k^{-1} \hat{\Theta}_{k-1} - \phi_k \phi_k^T \hat{\Theta}_{k-1} + \phi_k y_k \right) \\ &= \hat{\Theta}_{k-1} + P_k \phi_k \left(y_k - \phi_k^T \hat{\Theta}_{k-1} \right) = \hat{\Theta}_{k-1} + K_k \varepsilon \end{aligned} \tag{42}$$

Then the LS estimate can be given as

$$\begin{cases} \varepsilon_k = y_k - \phi_k^T \hat{\Theta}_{k-1} \\ \hat{\Theta}_k = \hat{\Theta}_{k-1} + K_k \varepsilon \\ K_k = P_k \phi_k \\ P_k = \left(P_{k-1}^{-1} + \phi_k \phi_k^T \right)^{-1} \end{cases} \tag{43}$$

where

$$\begin{aligned} P_k = \left(P_{k-1}^{-1} + \phi_k \phi_k^T \right)^{-1} &= P_{k-1} - P_{k-1} \phi_k \left[1 + \phi_k^T P_{k-1} \phi_k \right]^{-1} \phi_k^T P_{k-1} \\ &= P_{k-1} - \frac{P_{k-1} \phi_k \phi_k^T P_{k-1}}{1 + \phi_k^T P_{k-1} \phi_k} \end{aligned} \tag{44}$$

The iterative formula for the RLSM is given as follows:

$$\begin{cases} \varepsilon_k = y_k - \phi_k^T \hat{\Theta}_{k-1} \\ \hat{\Theta}_k = \hat{\Theta}_{k-1} + K_k \varepsilon \\ K_k = P_k \phi_k \\ P_k = P_{k-1} - \frac{P_{k-1} \phi_k \phi_k^T P_{k-1}}{1 + \phi_k^T P_{k-1} \phi_k} \end{cases} \tag{45}$$

4.3. The AVURPSO-RLS Parameter Identification

Although achieving accurate ranging in the AVURPSO algorithm is challenging, its global optimization capacity helps to narrow the solution range and approximate the optimal solution. The main drawback of the RLS is its sensitivity to the initial iteration value. However, when the initial value of the iteration is closer to the real solution, the RLS exhibits higher convergence speed and accuracy. Therefore, combining the global

optimization ability of AVURPSO with the fast convergence ability of the RLS in the neighborhood of the global optimal solution can help us achieve the desired results. The flowchart for finding the global optimal DSSR process based on the proposed AVURPSO-RLS algorithm is depicted in Figure 6.

Figure 6. The flowchart of the AVURPSO-RLS algorithm.

5. Case Study

5.1. Time Domain Simulation of DSSR

In this section, the suggested approach of AVURPSO-RLS is tested on an actual power grid in Hami City, China—a city with abundant new energy and coal energy resources on the Chinese mainland. Despite the abundance of new energy resources in this region, their shortcomings, such as their stochastic nature, volatility, and load distribution, present challenges for large-scale utilization. Generally, the wind speed here is greater than 4.38 m/s, and the effective wind speed is more than 2000 h. The typical output curve of wind energy in western China is shown in Figure 7.

Figure 7. Interannual variation curve of wind speed.

In addition, Hami is one of the major coal bases in China. It was the first UHVDC transmission channel in China to combine new energy with thermal electricity. The DIgSI-LENT/Power Factory software was used to develop and test the Hami power grid.

As can be seen in Figure 8, the three wind farm stations in this grid are Santanghu, Hami, and Yandun. This article analyzes three versions of the Hami Power Grid based on the geographic locations of wind farms.
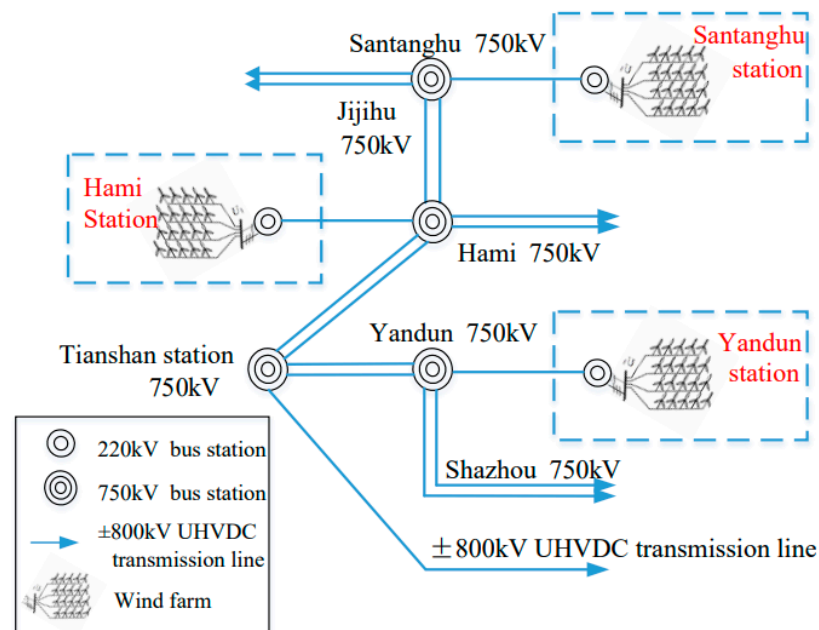
Figure 8. Schematic diagram of Hami power grid.

(1) Case 1: Santanghu station encompasses six wind farms and uses 220 kV wires to link the wind farms to its 750 kV station.

(2) Case 2: Three major wind farms (220 kV) are linked to the 750 kV central Hami station through three (220 kV) main wind farms.

(3) Case 3: Five (220 kV) primary wind farms are linked to the 750 kV Yandun station. Consequently, this paper discusses the three wind farms affiliated with the Hami Power Grid.

Figure 9 depicts the normal operating state curves (PV and QV curves) of the three wind farms. The figure displays the PV and QV curves at a certain time in the three cases of Hami power grid operation under normal conditions. As can be seen, the outputs of *P* and *Q* are within the stable voltage range [0.95~1.05].
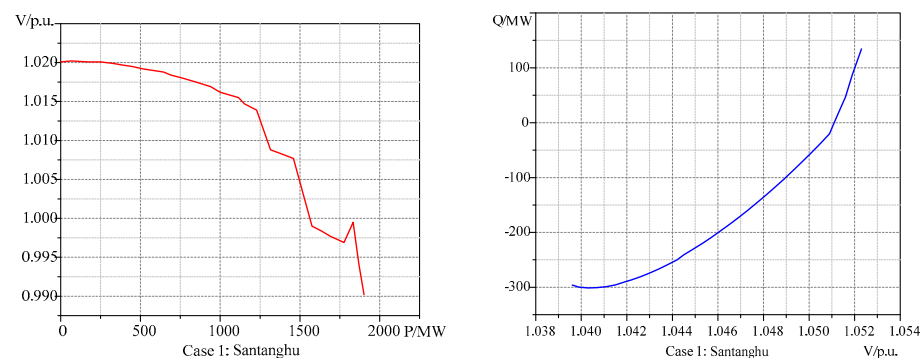
Figure 9. *Cont.*
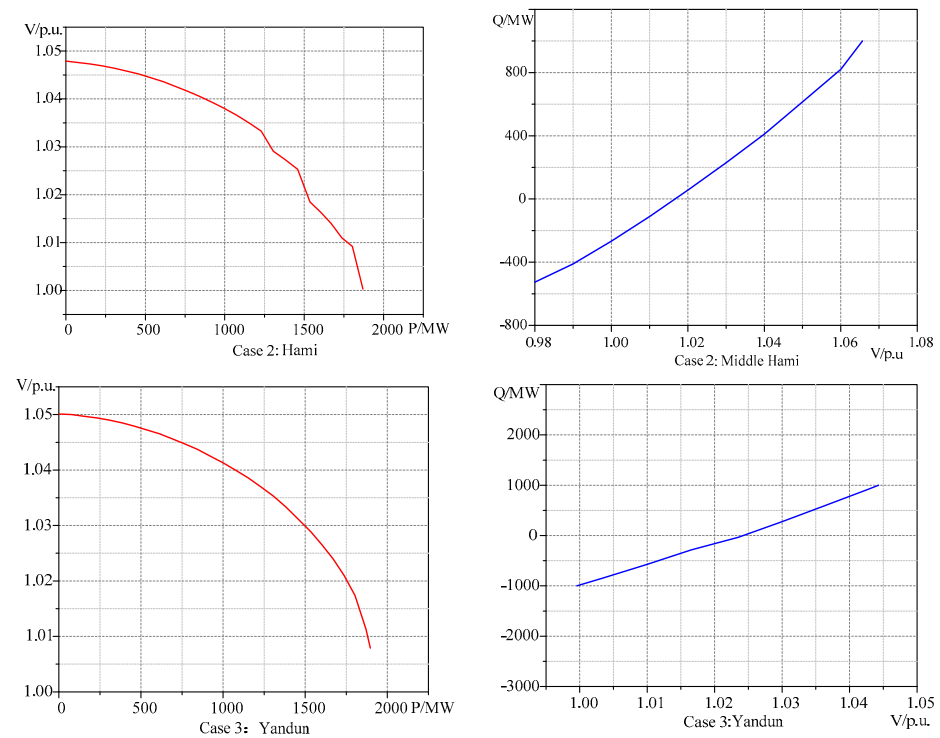
Figure 9. PV and QV curves of the three cases.

The bus B2 of the Hami power grid is intentionally subjected to a three-phase short-circuit fault. The fault is initiated at 1 s and cleared at 1.1 s. Figure 10 illustrates the equivalent dynamic response of the system. A three-phase short circuit fault occurs one minute after the system starts to operate. After the fault is removed, the system transitions to a new stable operating state through adjustment.
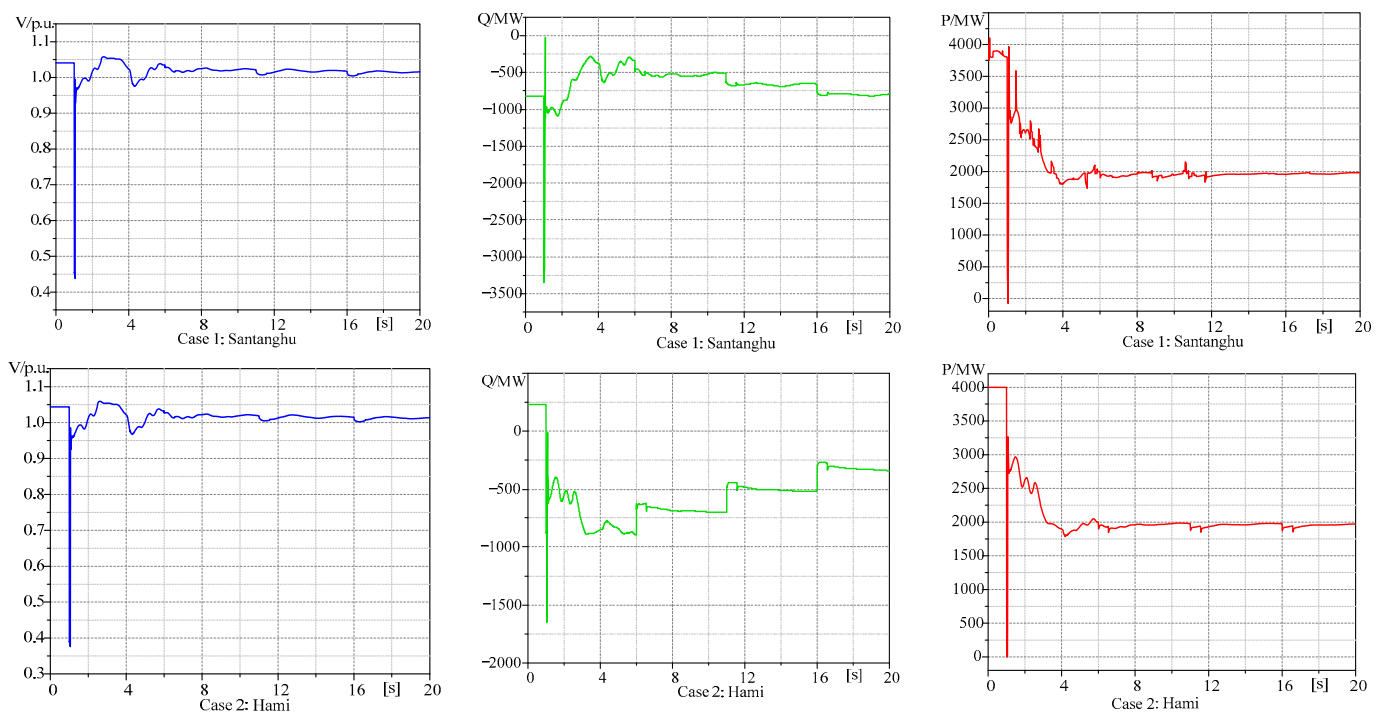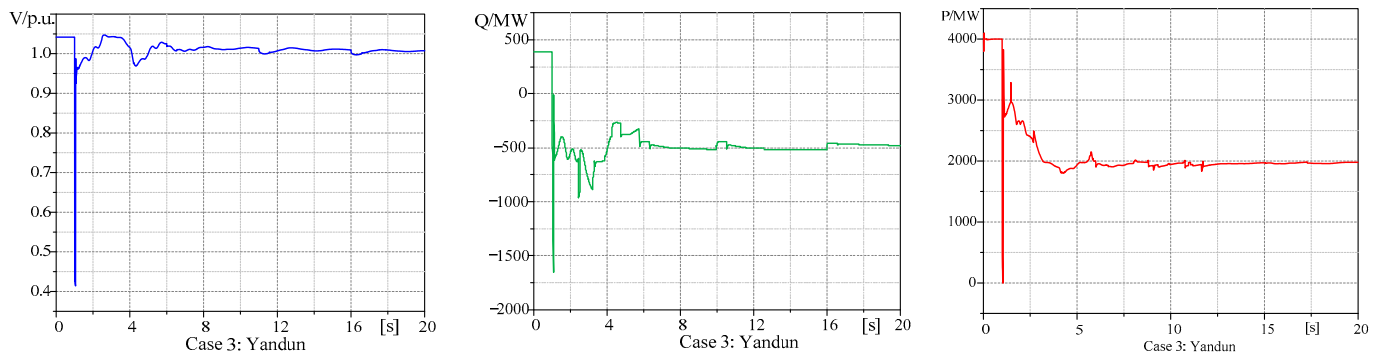

Figure 10. *Cont*.

Figure 10. N−1 simulation of the wind connection system at different stations (Case 1: Santanghu station; Case 2: Hami station; Case 3: Yandun station).

After the failure, the *P*, *Q*, and *V* all drop significantly at the same time. As the *P* stabilizes, the *V* rises, and the *Q* increases after the fault has been cleared.

Based on Figures 9 and 10, a two-dimensional security domain for three cases is obtained through the AVURPSO-RLS algorithm.

Boundary data can be obtained from the two-dimensional security and stability regions of the three cases shown in Figure 11, and the dynamic security and stability region of the system can be obtained via HP fitting.
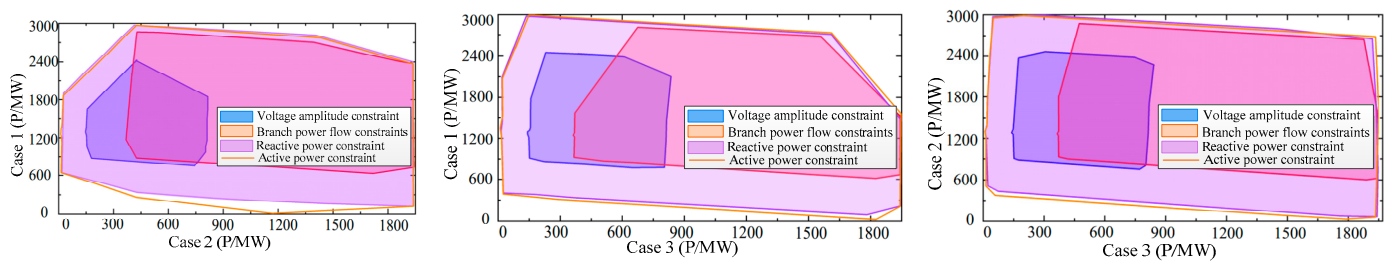
Figure 11. Two-dimensional SSR constructed by the IPSO-RLS hybrid algorithm (Case 1: Santanghu station; Case 2: Hami station; Case 3: Yandun station).

The HP approach can be used to match the DSSR boundary via extensive simulation computations, and the HP coefficients can be discovered using AVURPSO-RLS. Then, DIgSILENT/Power Factory simulation is utilized to derive the various *p* values of the three situations. Three of these examples' DSSRs are shown in Figure 12.
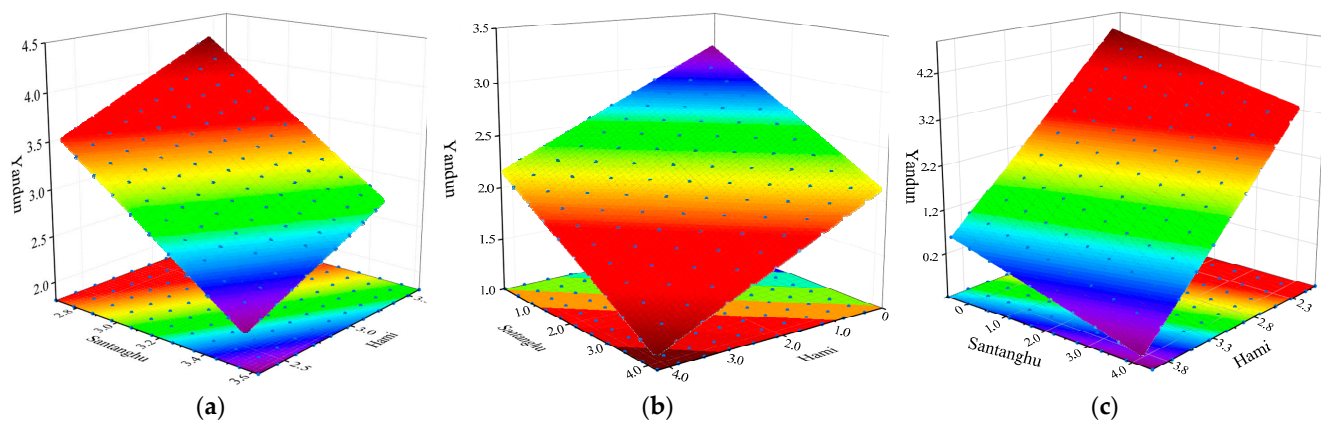
Figure 12. DSSRs of three cases with different power outputs (Case 1: Santanghu station; Case 2: Hami station; Case 3: Yandun station). (**a**) A 40% power output; (**b**) 70% power output; (**c**) ultimate output.

The *P* of the three regions is used as the research object to obtain the DSSR surface, as shown in Figure 12. For this study, in the DSSR plane, the yellow area shows where the system can operate safely and stably. The area extending from yellow to red and yellow to blue ensures the system's safe and stable operation. The dark red and dark blue areas allow the system to operate safely and stably under normal conditions, but their safety and stability may be reduced in cases of system failure. According to the above simulation, the active output limit in the Santanghu area is 1833.6 MW, that in Hami is 4742.22 MW, and that in Yandun is 5888.3 MW. Combined with the power flow calculation data, the active power margin K_p of each region is 5.7%, 65.4%, and 15.8%, respectively. The reactive power output limit in the Santanghu area is 2641.2 MW, while it is 1656.7 MW in the Hami area, and 827.0 MW the Yandun area. Combined with the tidal current calculation results, the reactive power margin K_Q values of each wind zone are 25.6%, 40.7%, and 37.1%, respectively. The voltage fluctuation amplitude in the Santanghu area is [0.44, 1.055], while it is [0.37, 1.06] in Hami and [0.42, 1.045] in Yandun. As the *P* of each region gradually increases beyond the limit, the operating point will also move to the upper part of the DSSR surface, and the wind farm may collapse, leading to insecurity in the entire Hami power grid. When the system's operating point is above the DSSR surface, excessive reactive power output in each region can easily cause an imbalance in the system's power.

The different proportions of the calculation error of the HP coefficient in the injection power space for the three cases are shown in Figure 13. When the injection power is 70%, the error of the HP coefficient is the smallest, and the fitting plane has high precision and reliability. The maximum fitting error of the boundary of the DSSR obtained by fitting is 4.56% (here, the error is defined as the maximum ratio of the coordinate component of the distance from the critical point to the fitting hyperplane to the coordinate component of the corresponding point on the hyperplane; that is, the percentage). All results meet the requirements of engineering precision.
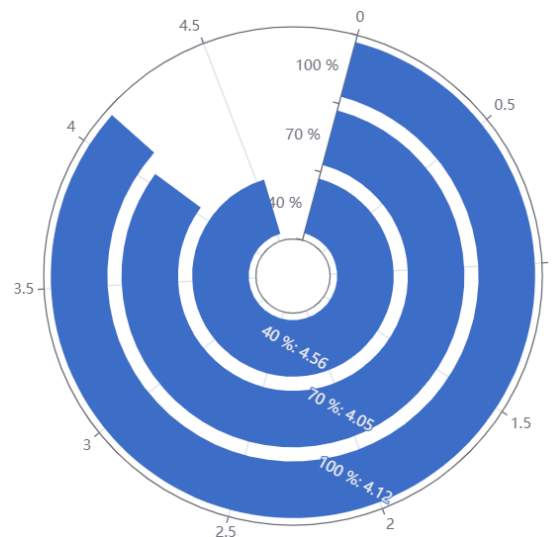

Figure 13. DSSR hyperplane fitting error with different power outputs.

To improve the efficiency when creating a DSSR boundary with a hyperplane expression, the AVURPSO-RLS technique is suggested as a viable alternative. The first step involves looking for critical points in an equivalent effective search space built from the key generators identified by the AVURPSO algorithm and the orthogonal point selection method. The second step involves using the RLS method to fit the hyper-plane coefficients of the DSSR boundary. Extensive simulation results regarding the Hami power grid demonstrate that the proposed technique is much more computationally efficient than the existing fitting method, without sacrificing accuracy.

5.2. Sensitivity Analysis of DSSR

Sensitivity analysis is used to verify whether the IPSO-RLS hybrid algorithm is applicable and whether the static security domain is stable, that is, whether previous analysis results will change when the research object undergoes minor changes. In actual analysis work, partial adjustments can be made to the analysis results based on changes in the analysis parameters, and new analysis results can be obtained without recalculation. In this paper, several representative critical points are selected to perform sensitivity analyses of ±10%, ± 20%, and ± 30% on the critical surfaces of the DSSR, respectively, in order to simulate fluctuations in wind speed. The results are shown in Figure 14.
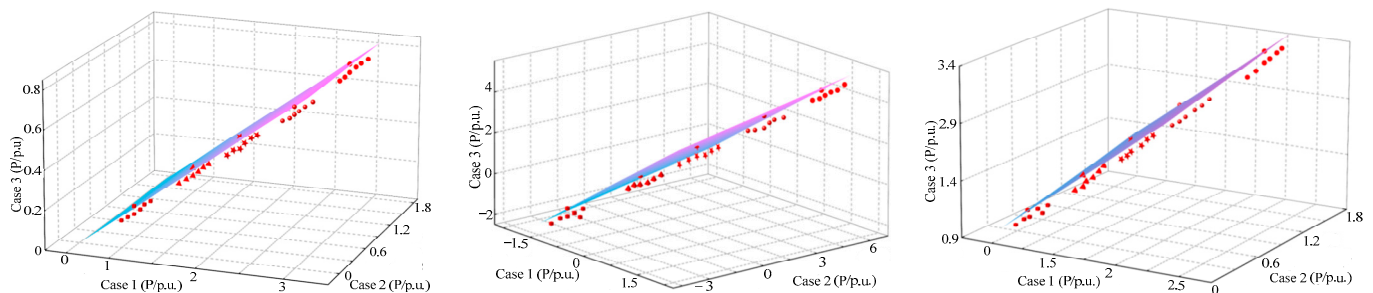
Figure 14. Sensitivity analysis of DSSR in three cases (Case 1: Santanghu station; Case 2: Hami station; Case 3: Yandun station).

When the operating points of the system under different outputs are within the DSSR and below the DSSR surface, the system is safe. Otherwise, the system is not secure. The sensitivity analysis results in Figure 14 indicate that the operating points corresponding to different sensitivity changes are within the limits of the output range of each wind farm group, and the entire system is still safe; that is, the DSSR surface is not sensitive to sensitivity changes. Therefore, the IPSO-RLS hybrid algorithm is reasonable and applicable for use in DSSR analysis.

5.3. Comparative Analysis of Algorithms

To verify the effectiveness and accuracy of the proposed AVURPSO algorithm, the error and convergence accuracy are compared with the genetic algorithm (GA), the different evolutional algorithm (DE), and the PSO algorithm. During the experimental verification, the control parameters of all algorithms are set according to Table 1.

Table 1. Control parameters of related algorithms.

Algorithms	Parameters	Value
GA	crossover rate	0.9
	mutation rate	0.01
PSO	inertia weight ω	-0.3236
	particle optimal weight, c_1	-0.1136
	group optimal weight, c_2	3.9789
DE	mutation factor, F	0.5
	crossover factor, CR	0.9

Figure 15 compares the convergence accuracies of the GA, PSO, DE, and AVURPSO algorithms when used in optimization. The error comparison results of the GA, PSO, DE, and AVURPSO algorithms are listed in Table 2.
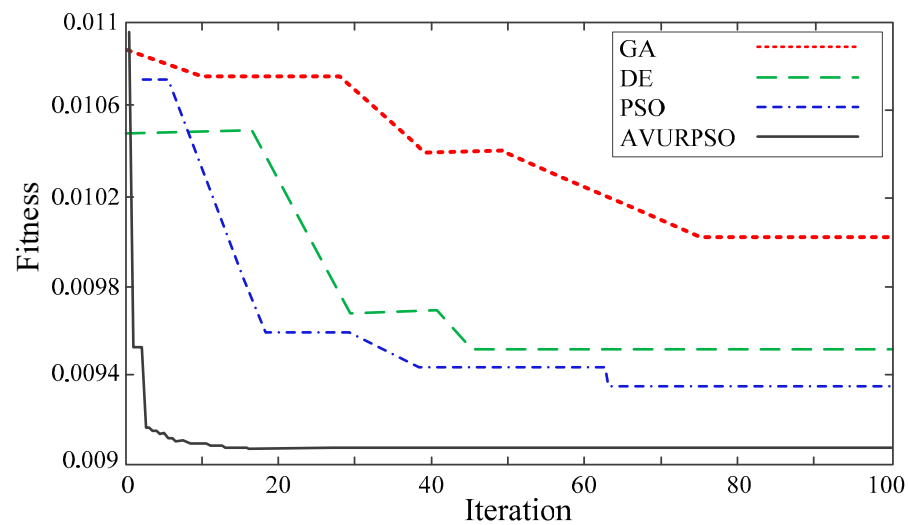
Figure 15. Average convergence accuracy of different algorithms.

Table 2. Error comparison of different algorithms.

Algorithms	Cases	Optimal Value	Worst Value	Average Value	Standard Deviation
GA	Case 1	0.000552	0.00099	0.000419	0.000238
	Case 2	0.0011	0.00258	0.259	0.0817
	Case 3	0.000424	0.000113	0.000456	0.000339
DE	Case 1	0.0311	0.0436	0.0153	0.0132
	Case 2	−9.6601	−9.6134	−9.6501	0.0182
	Case 3	−9.1140	−7.8072	−8.4778	0.3489
PSO	Case 1	0.7210	7.3193	3.3746	2.3257
	Case 2	0.0101	0.000278	0.031	0.875
	Case 3	0.0012	0.3378	0.1059	0.1330
AVURPSO	Case 1	0.0335	0.000203	0.326	0.0146
	Case 2	0.000487	0.0019	0.000378	0.000316
	Case 3	0.00463	0.00346	0.031	0.0028

The "best value", "worst value", "average value", and "standard deviation" in Table 2 represent the errors in the best value, the worst value, the average value, and the standard deviation value of the P obtained in the search space. The GA and DE algorithms cannot find the optimal error solution under the different conditions of new energy permeability. Although the results obtained by PSO are better than those obtained by the first two algorithms, the AVURPSO algorithm achieves higher accuracy with a smaller error. Therefore, it can be proven that the AVURPSO algorithm achieves the best performance in searching for the optimal solution.

The results show that the AVURPSO algorithm outperforms other algorithms in terms of accuracy, with its optimal solution (Best) being more accurate than those obtained by other algorithms. Additionally, AVURPSO exhibits a superior global or near-global optimal solution-searching ability. Moreover, the low standard deviation of the AVURPSO algorithm proves its stable consistency and higher convergence accuracy. The average global or near-global optimal solution yields a stable average P, further validating the AVURPSO algorithm's reliability in producing high-quality solutions.

Figure 15 demonstrates that the AVURPSO algorithm has better convergence accuracy than the GA, DE, and PSO algorithms. The training results of the AVURPSO algorithm

converge rapidly after 400 iterations, whereas the results of the PSO algorithm converge after 800 iterations. The GA algorithm seems to be the slowest, with an unstable and fluctuating iterative process, taking more time to converge successfully. Consequently, the AVURPSO algorithm is more efficient, and its strong exploration ability effectively overcomes its premature convergence and maintains its convergence speed.

The results in Figure 16 show that the AVURPSO algorithm takes less time to iterate, and is faster than the DE, GA, and PSO algorithms. The AVURPSO algorithm is more precise and faster in terms of convergence. In addition, the AVURPSO algorithm also shows improved precision in SSR compared with PSO.
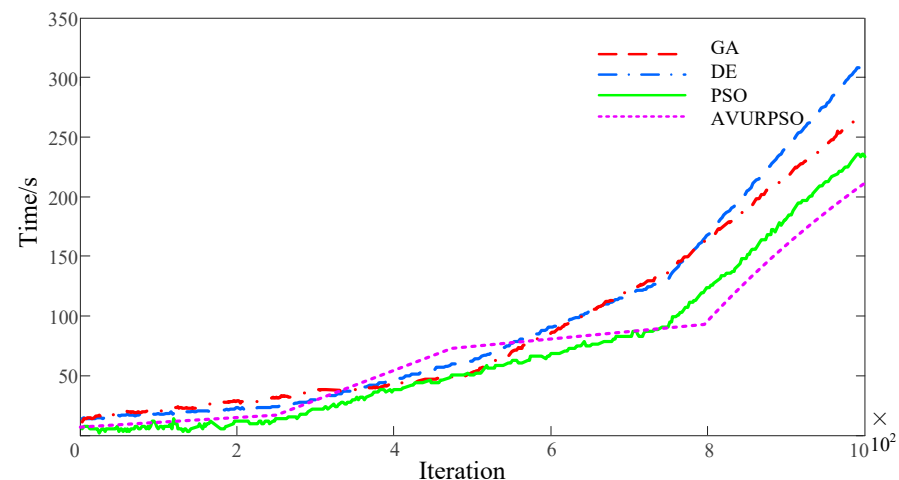
Figure 16. Iteration times of different algorithms.

6. Conclusions

This paper proposes the concepts and a model of the new energy power system DSSR. Since the operating parameters can be maintained within the constraints of the new energy DSSR, areas where operating parameter verifications can be simplified were further established, and this could improve the calculation speed. Then, a security and stability analysis framework for a new regional energy power system based on the DSSR was given. Based on the DSSR, a model for optimizing control was presented to adjust the system's security status. The case study has verified the effectiveness of the security region and realized its visualization in a three-dimensional space. Furthermore, the secure operating point could be optimized to enhance the security and efficiency status under optimizing control. The proposed method pushes forward the process of the practical application of DSSR to enhance situational awareness, considering the uncertainty of new energy. In the future, the impact of the load can be further considered, and advanced data-driven methods can be further explored to improve the efficiency.

Based on the facts that HPs can approximate the boundaries of the practical SR in the power injection space, and that the SR is irrelevant to the operation state, the great advantages of the SR method when used in security monitoring, probabilistic security (risk) assessment, and the optimization of power systems have been discovered. Compared to the fitting method, the SR method significantly improves the computational speed. In addition, it achieves the accuracy required of practical engineering applications that require many simulations to search for their many critical points. In the future, the SR methodology will continue to be a powerful tool used in the security analysis of smart grids with massive and uncertain distributed generation capacities. Moreover, the SR methodology is a powerful tool for improving situation awareness, since it can make visualizations easier to construct, and enables the rapid determination of the security margin.

References

1. Zhu, H.; Goh, H.H.; Zhang, D.; Ahmad, T.; Liu, H.; Wang, S.; Li, S.; Liu, T.; Dai, H.; Wu, T. Key technologies for smart energy systems: Recent developments, challenges, and research opportunities in the context of carbon neutrality. *J. Clean. Prod.* **2022**, *331*, 129809. [CrossRef]
2. You, Y.; Yi, L. Energy industry Carbon neutrality transition path: Corpus-based AHP-DEMATEL system modelling. *Energy Rep.* **2022**, *8*, 25–39. [CrossRef]
3. Shabani, H.R.; Kalantar, M. Real-time transient stability detection in the power system with high penetration of DFIG-based wind farms using transient energy function. *Int. J. Elect. Power Energy Syst.* **2021**, *133*, 107319. [CrossRef]
4. Boričić, A.; Torres, J.L.R.; Popov, M. Fundamental study on the influence of dynamic load and distributed energy resources on power system short-term voltage stability. *Int. J. Elect. Power Energy Syst.* **2021**, *131*, 107141. [CrossRef]
5. Adetokun, B.B.; Muriithi, C.M.; Ojo, J.O. Voltage stability assessment and enhancement of power grid with increasing wind energy penetration. *Int. J. Elect. Power Energy Syst.* **2020**, *120*, 105988. [CrossRef]
6. Wang, J.; Xu, J.; Liao, S.; Sima, L. Coordinated Optimization of Integrated Electricity-Gas Energy System Considering Uncertainty of Renewable Energy Output. *Auto. Elect. Power Syst.* **2019**, *43*, 2–9.
7. Dong, X.; Tang, Y.; Bu, G.; Shen, C.; Song, G.; Wang, Z.; Zhao, B. Confronting problem and challenge of large-scale AC-DC hybrid power grid operation. *Proc. Chin. Soc. Electr. Eng.* **2019**, *39*, 3107–3119.
8. Li, B.; Chao, P.; Li, W.; Xu, S.; Liu, X.; Li, Z. Transient overvoltage calculation method of wind power transmission system via UHVDC. *Electr. Mach. Control.* **2021**, *25*, 11–18.
9. Tu, J.; Zhang, J.; Liu, M.; Yi, J.; He, Q. Study on Wind Turbine Generators Tripping Caused by HVDC Contingencies of Wind-Thermal-Bundled HVDC Transmission Systems. *Power Syst. Technol.* **2015**, *39*, 3333–3338.
10. Wu, Y.; Hu, M.; Liao, M.; Liu, F.; Xu, C. Risk assessment of renewable energy-based island microgrid using the HFLTS-cloud model method. *J. Clean. Prod.* **2021**, *284*, 125362. [CrossRef]
11. Hnyilicza, E.; Lee, S.; Schweppe, F.C. Steady-state security regions: Set-theoretic approach. *IEEE Trans. Circuits Syst.* **1982**, *29*, 703–711.
12. Jarjis, J.; Galiana, F.D. Quantitative analysis of steady state stability in power networks. *IEEE Trans. Power Appar. Syst.* **1981**, *1*, 318–326. [CrossRef]
13. Phillipe, V.G.; Saraiva, J.T. State-of-the-art of transmission expansion planning: A survey from restructuring to renewable and distributed electricity markets. *Int. J. Elect. Power Energy Syst.* **2019**, *111*, 411–424.
14. Maihemuti, S.; Wang, W.; Wang, H.; Wu, J. Voltage Security Operation Region Calculation Based on Improved Particle Swarm Optimization and Recursive Least Square Hybrid Algorithm. *J. Mod. Power Syst. Clean Energy* **2021**, *9*, 138–147. [CrossRef]
15. Lin, W.; Jiang, H.; Yang, Z. Time-line security regions in high dimension for renewable accommodations. *arXiv* **2022**, arXiv:2201.01019.
16. Zeng, Y.; Yu, Y. A practical direct method for determining dynamic security regions of electrical power systems. *Proc. Int. Conf. Power Syst. Tech.* **2002**, *2*, 1270–1274.

17. Xue, A.; Wu, F.F.; Lu, Q.; Mei, S. Power System Dynamic Security Region and Its Approximations. *IEEE Trans. Circ. Syst.* **2006**, *53*, 2849–2859. [CrossRef]

18. Yu, Y.; Liu, Y.; Qin, C.; Yang, T. Theory and Method of Power System Integrated Security Region Irrelevant to Operation States: An Introduction. *Engineering* **2020**, *6*, 754–777. [CrossRef]

19. Zhang, Q.; Zheng, H.; Wang, J.; Liu, X.; Qu, Y.; Bie, Z. A method for calculating static voltage stability margin of power system based on aq bus. *Power Syst. Technol.* **2019**, *43*, 714–721.

20. Xia, S.; Bai, X.; Chen, S.; Guo, Z.; Xu, Y. Solving for dynamic security region based on Taylor series trajectory sensitivity. *Electr. Power Autom. Equip.* **2018**, *38*, 157–164.

21. Pourbehzadi, M.; Niknam, T.; Aghaei, J.; Mokryani, G.; Shafie-Khah, M.; Catalão, J.P.S. Optimal operation of hybrid AC/DC microgrids under uncertainty of renewable energy resources: A comprehensive review. *Int. J. Elect. Power Energy Syst.* **2019**, *109*, 139–159. [CrossRef]

22. Javadian, S.; Haghifam, M.-R.; Firoozabad, M.F.; Bathaee, S. Analysis of protection system's risk in distribution networks with DG. *Int. J. Electr. Power Energy Syst.* **2013**, *44*, 688–695. [CrossRef]

23. Yu, Y.; Luan, W. Practical dynamic security region of power system. *Proc. CSEE* **1990**, *13*, 14–22.

24. Yu, Y.; Lin, J. Practical analytic expression of power system dynamic security region's boundary. *J. Tianjin Univ.* **1997**, *30*, 1–8.

25. Zeng, Y.; Fan, J.C.; Yu, Y.X. Practical dynamic security regions of bulk power system. *Auto. Elec. Power Syst.* **2001**, *25*, 6–10.

26. Min, L.; Yu, Y.X.; Lee, S.; Pei, T. Identification method of Instability modes and its application in dynamic security region. *Auto. Electr. Power Syst.* **2004**, *28*, 28–32.

27. Feng, Z.; Yu, Y.; Zeng, Y. An Intercept method for determining practical dynamic security regions of power systems. *Auto. Electr. Power Syst.* **2006**, *30*, 18–22.

28. Zeng, Y.; Yu, Y.X.; Jia, H.J. Computing practical dynamic security region by technology of power sensitivity analysis. *J. Tianjin Univ.* **2006**, *39*, 76–82.

29. Qin, C.; Liu, Y.L.; Yu, Y.X. Dynamic security region of power systems with double fed induction generator. *Trans. China Electro. Tech. Soc.* **2015**, *30*, 157–163.

30. Hou, K.F.; Yu, Y.X.; Lee, S.T.; Pei, Z. Reduction and reconstruction of power system practical dynamic security region. *Auto. Electr. Power Syst.* **2004**, *28*, 16–21.

31. Russell, S.J.; Norvig, P. *Artificial Intelligence: A Modern Approach*; Pearson Education Limited: London, UK, 2016.

32. Movahedi, A.; Niasar, A.H.; Gharehpetian, G.B. Optimal real-time operation strategy for microgrid: An ADP-based stochastic nonlinear optimization approach. *IEEE Trans Sustain. Energy* **2019**, *10*, 931–942.

33. Movahedi, A.; Niasar, A.H.; Gharehpetian, G.B. Designing SSSC, TCSC, and STATCOM controllers using AVURPSO, GSA, and GA for transient stability improvement of a multi-machine power system with PV and wind farms. *Int. J. Electr. Power Energy Syst.* **2019**, *106*, 455–466. [CrossRef]